PHYSICAL REVIEW B **108**, 195149 (2023)

Ab initio insights on the ultrafast strong-field dynamics of anatase TiO_2

Sruthil Lal S. B.,[1] Lokamani,[2] Kushal Ramakrishna,[3,2] Attila Cangi,[3,2] D. Murali,[4] Matthias Posselt,[2]
Assa Aravindh Sasikala Devi,[5] and Alok Sharan[1,*]
[1]*Department of Physics, Pondicherry University, R. V. Nagar, Kalapet, Puducherry 605014, India*
[2]*Helmholtz-Zentrum Dresden-Rossendorf, 01328 Dresden, Germany*
[3]*Center for Advanced Systems Understanding, 02826 Görlitz, Germany*
[4]*Indian Institute of Information Technology Design and Manufacturing (IIITDM), Kurnool, Andhra Pradesh 518007, India*
[5]*Nano and Molecular Systems Research Unit, University of Oulu, P.O.Box 8000, FI-90014, Oulu, Finland*

(Received 27 June 2023; revised 28 September 2023; accepted 2 November 2023; published 27 November 2023)

Electron dynamics of anatase TiO_2 under the influence of ultrashort and intense laser field is studied using the real-time time-dependent density functional theory (TDDFT). Our findings demonstrate the effectiveness of TDDFT calculations in modeling the electron dynamics of solids during ultrashort laser excitation, providing valuable insights for designing and optimizing nonlinear photonic devices. We analyze the perturbative and nonperturbative responses of TiO_2 to 30 fs laser pulses at 400 and 800 nm wavelengths, elucidating the underlying mechanisms. At 400 nm, ionization via single photon absorption dominates, even at very low intensities. At 800 nm, we observe ionization through two-photon absorption within the intensity range of 1×10^{10} to 9×10^{12} $\mathrm{W/cm^2}$, with a transition from multiphoton to tunneling ionization occurring at 9×10^{12} $\mathrm{W/cm^2}$. We observe a sudden increase in energy and the number of excited electrons beyond 1×10^{13} $\mathrm{W/cm^2}$, leading to their saturation and subsequent laser-induced damage. We estimate the damage threshold of TiO_2 for 800 nm to be 0.1 $\mathrm{J/cm^2}$. In the perturbative regime, induced currents exhibit a phase shift proportional to the peak intensity of the laser pulse. This phase shift is attributed to the intensity-dependent changes in the number of free carriers, indicative of the optical Kerr effect. Leveraging the linear dependence of phase shift on peak intensities, we estimate the nonlinear refractive index (n_2) of TiO_2 to be 3.54×10^{-11} $\mathrm{cm^2/W}$.

DOI: 10.1103/PhysRevB.108.195149

I. INTRODUCTION

Time-dependent density-functional theory (TDDFT) [1] describes the quantum dynamics of electrons under the influence of a time-dependent external potential [2–7]. TDDFT calculations are used to study ultrashort laser-matter interactions including high-harmonic generation (HHG) [8–11], nonlinear current injection [12,13], formation of Floquet-Bloch states [14,15], and laser ablation [16,17]. TDDFT computations have also been utilized to distinguish between the purely electronic and phononic contribution to nonequilibrium dynamics in metals caused by lasers [18]. Furthermore, TDDFT has been applied to study the influence of the laser pulse widths in the formation of nitrogen-vacancy centers in the diamond lattice [19].

The strong-field response in solids has become an area of renewed interest due to recent experimental evidence that dielectrics can survive electric fields approaching their critical fields when exposed to laser pulses shorter than the electronic relaxation time scales [20–22]. Initiating, driving, and probing the nonlinear electron dynamics in crystalline materials is now possible with optical subcycle resolutions, opening the door for optical field-effect devices operating within single optical cycles and petahertz signal processing [21–29]. For instance, a reversible energy exchange at sub-30-attosecond time scales was observed in fused silica by Sommer *et al.* [28]. Under the influence of strong electric fields, it has been shown that the ac conductivity of fused silica increases by 18 orders of magnitude within one femtosecond [24] and is completely reversible. TDDFT calculations have shown that electron tunneling is the fundamental mechanism of carrier injection in silica under few-cycle extreme ultraviolet (XUV) illumination [27]. Materials undergo dynamic metallization [23,30–32] when irradiated with optical pulses of amplitude as large as 1 V/Å. This observation was also supported by TDDFT calculations [12].

TDDFT calculations of ultrashort laser-induced electron dynamics for nonlinear photonic applications have so far been focused on Si [16,27], SiO_2 [4,16,32], linear carbon chain [33], diamond [2,34–36], phospherene [37], and MoS_2 [38]. Titanium dioxide (TiO_2), commonly used as a saturable absorber in passively Q-switched fiber lasers [39,40], has great potential for enabling nonlinear photonics. The nonlinear optical response of anatase TiO_2 has a typical recovery period of approximately 1.5 ps [41]. The nonlinear index (n_2) of bulk and thin film of TiO_2 ranges from $(0.8–3)\times10^{-14}$ $\mathrm{cm^2/W}$ [42–44], which is greater than the nonlinear index of silica fiber (2.48×10^{-16} $\mathrm{cm^2/W}$ [45]). Moreover, the two-photon absorption of TiO_2 at 800 nm is minimal, making it ideal for waveguides operating near 800 nm [46]. TiO_2 can be formed at low temperatures (<400 °C) and offers advantages

---

[*] aloksharan@gmail.com

over silicon nitride with its higher refractive index (2.4 vs 2.0) and more than three times stronger Kerr nonlinearity [42,47,48]. These properties enable back-end integration with silicon microphotonic devices. Existing estimates of n_2 of TiO_2 are either from femtosecond z-scan measurements or by fitting the nonlinear pulse propagation simulations (based on the nonlinear Schrödinger equation) to the experimental data [49]. A systematic analysis of ultrafast nonlinear optical interactions in TiO_2 from a microscopic perspective has yet to be explored.

This study uses first-principle simulations to examine the microscopic electron dynamics of crystalline anatase TiO_2 modulated by an ultrashort and intense laser fields. We employ TDDFT calculations as implemented in the software package OCTOPUS [50]. We explore the response of anatase TiO_2 to 800 nm and 400 nm laser pulses with intensities spanning from the perturbative to strong-field regimes (nonperturbative). Different regimes of nonlinear interactions with the external electric field are characterized, and various underlying mechanisms are analyzed. The evolution of photoinduced current and energy transfer during the interaction is studied. We determine the nonlinear refractive index and optical damage threshold of anatase TiO_2 and our results are in excellent agreement with previously reported experimental data.

The paper is organized as follows. Section II describes the computational methods employed for determining the photoinduced current and the energy dynamics of TiO_2. The results and analysis of our study are discussed in Sec. III, where we also compare them with the existing experimental data. We conclude the paper with a summary in Sec. IV.

II. COMPUTATIONAL METHODS

A. Time-dependent density functional theory

The electron dynamics in a unit cell of a periodic crystal driven by a time-dependent electric field $\boldsymbol{E}(\boldsymbol{r},t)$ is described in terms of the time-dependent Kohn-Sham (KS) equations

$$i\frac{\partial}{\partial t}u_{n,k}(\mathbf{r},t)=\left\{\frac{1}{2}[\mathbf{p}+\mathbf{A}_{\mathrm{S}}(\boldsymbol{r},t)]^2+v_{\mathrm{S}}(\boldsymbol{r},t)\right\}u_{n,k}(\boldsymbol{r},t),\quad(1)$$

where $u_{n,k}(\boldsymbol{r},t)$ denotes KS orbitals with the band index n, the electron wave vector k, and $v_{\mathrm{S}}[n](\boldsymbol{r},t)=v_{\mathrm{ion}}(\boldsymbol{r},t)+v_{\mathrm{H}}[n](\boldsymbol{r},t)+v_{\mathrm{XC}}[n](\boldsymbol{r},t)$ is the KS potential with v_{ion} denoting the external ionic potential, v_{H} the Hartree potential, and v_{XC} the exchange-correlation (XC) potential. Furthermore, $\mathbf{p}$ is the momentum operator and $\mathbf{A}_{\mathrm{S}}(\boldsymbol{r},t)=\mathbf{A}(\boldsymbol{r},t)+\mathbf{A}_{\mathrm{XC}}(\boldsymbol{r},t)$ is the vector potential composed of the applied vector potential $\mathbf{A}(\boldsymbol{r},t)$ and an XC contribution $\mathbf{A}_{\mathrm{XC}}(\boldsymbol{r},t)$ [51]. The applied vector potential represents an applied electromagnetic field, such as a laser pulse, and is related to the applied electric field by $\boldsymbol{E}(\boldsymbol{r},t)=-(1/c)[\partial\mathbf{A}(\boldsymbol{r},t)/\partial t]$. Note that the laser pulse can be treated as spatially uniform $\boldsymbol{E}(t)$ under the dipole approximation. Solving the time-dependent KS equations with the exact XC potential and XC vector potential yields the exact time-dependent electron density $n(\boldsymbol{r},t)=\sum_{n,\mathbf{k}}^{occ}u^*_{n,k}(\boldsymbol{r},t)\,u_{n,k}(\boldsymbol{r},t)$. However, in practice approximations are used, e.g., a particular approximation is used to express the XC potential [52], the adiabatic approximation is applied, and the A_{XC} is often neglected. We follow the general practice by applying these approximations as detailed below. Note that we adopt Hartree atomic units, i.e., $\hbar=e=m=1$.

Another useful quantity is the microscopic current density which is determined in the outlined framework as

$$\boldsymbol{j}(\boldsymbol{r},t)=\sum_{n\mathbf{k}}^{occ}\frac{1}{2}\{u^*_{n,k}(\boldsymbol{r},t)[\mathbf{p}+\boldsymbol{A}(t)]u_{n,k}(\boldsymbol{r},t)\},\quad(2)$$

where the summation runs over the occupied bands. The macroscopic current density $J(t)$ along the laser polarization direction $\boldsymbol{E_0}$ is obtained by averaging $\boldsymbol{j}(\boldsymbol{r},t)$ over the unit cell with volume Ω,

$$J(t)=\frac{1}{\Omega}\int_{\Omega}d^3\boldsymbol{r}\,\boldsymbol{j}(\boldsymbol{r},t)\cdot\boldsymbol{E_0}/|\boldsymbol{E_0}|.\quad(3)$$

The polarization density corresponding to $J(t)$ is $P(t)=\int_0^t J(t')dt'$. The time-resolved energy density $W(t)$ transferred between the field and the material is evaluated by

$$W(t)=\int_{-\infty}^{t}dt'\,\boldsymbol{E}(t)\cdot\boldsymbol{J}(t).\quad(4)$$

Its resultant value at the end of the laser pulse $W(t\rightarrow\infty)$ determines the total amount of energy dissipated during the light-matter interaction. The number of electrons excited from the valence band to the conduction band N_{exc} per unit cell is calculated using [53]

$$N_{\mathrm{exc}}(t)=\sum_{n,n',\boldsymbol{k}}[\delta_{nn'\mathbf{k}}-|\langle u_{n,k}(0)|u_{n',k}(t)\rangle|^2].\quad(5)$$

Here $u_{n,k}(0)$ is the KS orbital of the initial state, $u_{n'k}(t)$ is the time-dependent KS orbital, and δ is the Kronecker delta.

We use the real-space, real-time code OCTOPUS [50] to carry out the TDDFT calculations. The laser-induced dynamics of valence electrons are calculated in a unit cell of anatase TiO_2. Anatase TiO_2 crystallizes with a tetragonal unit cell having a lattice spacing $a=3.79$ Å and $c/a=2.55$ [54–57]. We treat the interaction $v_{\mathrm{ion}}(\boldsymbol{r},t)$ between valence electrons and the ionic core by the Kleinman-Bylander pseudopotential [58]. The generalized gradient approximation (GGA) based on the Perdew-Burke-Ernzerhof functional (PBE) [59] is employed for the XC potential. KS orbitals are represented on the discretized real-space grid with $\Delta x=\Delta y=0.12$ Å and $\Delta z=0.20$ Å. It is equivalent to a plane-wave cutoff at 900 eV. The time-dependent KS equations are solved on a uniform grid with ≈29000 grid points. The Brillouin zone is uniformly sampled by $12\times12\times4$ Monkhorst-Pack grids [60]. The discretization consists of 363 symmetry-reduced k points for x polarized light. With this setup, the system's total energy converges to within 1 meV.

First, the ground state of TiO_2 is calculated, which will be used as the initial state for the time-dependent calculations. We then time propagate the KS orbital by solving Eq. (1) in the time domain. The time evolution is calculated with the approximated enforced time-reversal symmetry (AETRS) [61] as the time-evolution propagator with a time step $\Delta t=0.02$ a.u. The total simulation duration is 30 fs (1240 atomic units with a step size of 0.02 a.u., i.e., ≈64000 time steps). Note that, during the time evolution, ions are at their equilibrium positions in the ground state. Furthermore, the adiabatic approximation [62] is used, which means that the time

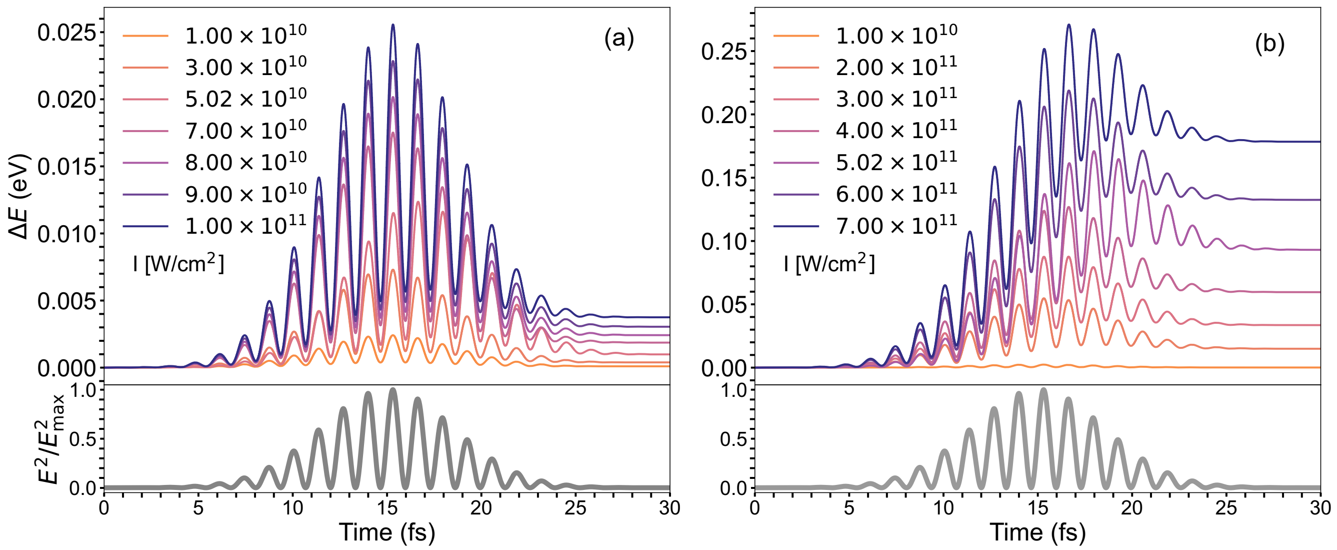

FIG. 1. Time-dependent energy exchanged between anatase TiO_2 and 30 fs pulses at 800 nm is given for different peak intensities. Panel (a) represents the nonresonant virtual energy transfer where the transferred energy oscillates synchronously $\boldsymbol{E}^2(t)$ (bottom panel). This occurs for intensities below 1×10^{11} W/cm^2. Panel (b) shows the energy exchange via resonant two-photon absorption for intensities ranging from 2×10^{11} to 7×10^{11} W/cm^2. For panels (a) and (b) the dynamics at 1×10^{10} W/cm^2 is shown as the reference.

dependence of the XC potential is approximated by evaluating a ground-state XC functional at the time-dependent density.

We calculate the response of TiO_2 to a linearly polarized laser pulse, which is represented by the spatially uniform electric field through the corresponding vector potential

$$\mathbf{A}(t) = \frac{\boldsymbol{E_0}}{\omega} \exp\left[\frac{-(t-t_0)^2}{2\tau_0^2}\right] \cos(\omega t), \tag{6}$$

where ω is the central frequency of the laser pulse and $\boldsymbol{E_0}$ is the amplitude of the time-dependent electric field $\boldsymbol{E}(t)$, which is related to the laser peak intensity $I_0 = c|\boldsymbol{E_0}|^2/8\pi$.

III. RESULTS

The following section presents the electron dynamics of crystalline anatase TiO_2 excited by 800 nm and 400 nm laser pulses represented by Eq. (6). The duration of the pulse is set to $T = 30$ fs ($\approx$12 fs at the FWHM of the envelope), while the amplitude of the pulse is varied from 10^7 to 10^{16} W/cm^2. The laser field is polarized along the x axis.

A. Energy transfer dynamics

The energy transferred from the applied electric field to anatase TiO_2 is evaluated by Eq. (4). Figure 1 shows the resultant energy dynamics for incident laser pulses at 800 nm ($\hbar\omega = 1.55$ eV) with different peak intensities. The central frequency of the pulse corresponds to energy lower than the direct gap (2.25 eV) [63], leading to two general types of temporal energy transfer profiles. The first type is nonresonant excitation. The transferred energy, in this case, oscillates synchronously with the $\boldsymbol{E}^2(t)$, and the system almost returns to the ground state at the end of the pulse. This represents a virtual energy transfer from the laser pulse to the electrons. Such dynamics is observed in Fig. 1(a) for peak intensities from 1×10^{10} to 1×10^{11} W/cm^2. This behavior is typical when the frequency is below the band gap and the intensity is very low.

The second kind of response is resonant excitation, where, along with the virtual oscillations, the transferred energy gradually increases during the pulse and persists beyond the pulse width. Given the pulse energy is below the band gap, this occurs when the field is strong enough to induce real excitation through multiphoton absorption. Figure 1(b) illustrates the energy transfer $W(t)$ for this scenario, observed for intensities ranging from 2×10^{11} to 7×10^{11} W/cm^2. The permanent energy transfer is related to creating electron-hole pairs, corresponding to the population transfer from valence bands to conduction bands.

Figure 2 illustrates the residual excitation energy (ΔE_{ex}) of anatase TiO_2 following interactions with 800 and 400 nm laser pulses, each at different peak intensities. The energy absorbed at 400 nm scales linearly to the intensity of the light, fitting exceptionally well with the expression $\Delta E_{ex} \propto I$ governing single-photon absorption (black dashed line in Fig. 2). This relation remains valid for light intensities of up to 5×10^{11} W/cm^2. The anticipated linear absorption pattern at 400 nm is because a single photon carrying 3.10 eV of energy bridges the direct band gap of anatase TiO_2. In contrast, single photon absorption below the direct band gap is unlikely at 800 nm and, hence, no permanent energy transfer for intensities below 1×10^{10} W/cm^2. However, as the intensity increases from 1×10^{10} W/cm^2 up to 1×10^{12} W/cm^2, the deposited energy at 800 nm increases, closely following a quadratic dependence ($\Delta E_{ex} \propto I^2$) represented by the red dashed line in Fig. 2.

At approximately 1×10^{13} W/cm^2 intensity, the excitation energies of 400 nm and 800 nm wavelengths combine to form a single curve. Below the intersection point, it displays a perturbative behavior and can be effectively modeled by I^N as discussed above, where I represents the laser intensity and N corresponds to the number of photons required to exceed the band gap energy. At intensities above the intersection

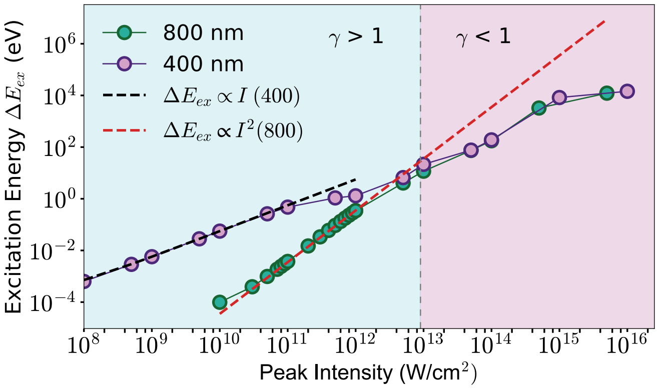

FIG. 2. Dependence of anatase TiO$_2$'s excitation energy (ΔE_{ex}) on the peak intensity during its interaction with 800 and 400 nm laser pulses: energy exchange at 400 nm is predominantly through single photon absorption for intensities up to $\approx 5 \times 10^{11}$ W/cm^2, represented by a linear fit to the expression $\Delta E_{ex} \propto I$. For 800 nm pulse, no energy is exchanged until peak intensity becomes $\geqslant 1 \times 10^{10}$, while energy exchange due to two-photon absorption becomes dominant for intensities ranging from 1×10^{10} W/cm^2 up to 1×10^{12} W/cm^2 ($\Delta E_{ex} \propto I^2$). For intensities larger than $\approx 1 \times 10^{12}$ W/cm^2, excitation energy no longer follows a quadratic dependence on the intensity due to the onset of tunneling ionization and absorption by secondary electrons. Typical intensity ranges of 800 nm pulses over which the multiphoton absorption ($\gamma > 1$) or tunneling ionization ($\gamma < 1$) becomes the dominant process are highlighted.

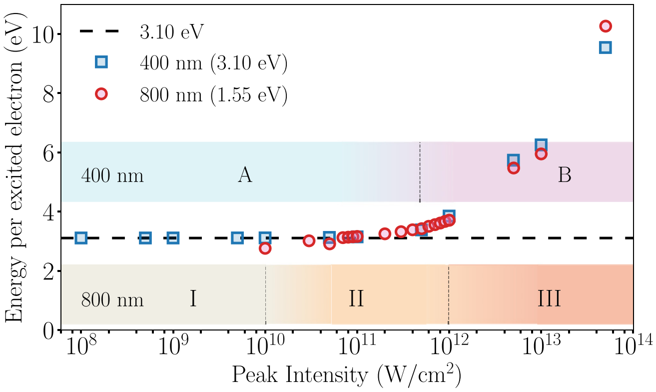

FIG. 3. Energy per excited electron (E^e_{res}) at 800 nm and 400 nm beyond the laser pulse is shown along with dominant excitation regimes highlighted in colored boxes. The color gradient at the boundary between the two regions implies the coexistence of multiple excitation mechanisms. In region A for 400 nm, E^e_{res} is 3.10 eV for intensities up to $\approx 1 \times 10^{12}$ W/cm^2, indicating single photon absorption. In region B, secondary excitation of excited electrons causes a substantial increase in E^e_{res}. At 800 nm, single photon absorption is unlikely for $I_0 \leqslant 1 \times 10^{10}$ W/cm^2 (region I). For intensities ranging from 1×10^{10} W/cm^2 to 1×10^{12} W/cm^2 (region II) energy per electron lies on the two-photon absorption energy (3.10 eV). E^e_{res} gradually increases and becomes frequency independent for intensities larger than $\approx 1 \times 10^{12}$ W/cm^2, potentially due to higher-order multiphoton absorption and secondary excitation of excited electrons (region III).

region, the excitation energy is independent of laser frequency and the curve's slope decreases compared to the region below the intersection [4]. This suggests a saturationlike behavior occurring in the material's response. The similarity of the number density of excited electrons for both 800 nm and 400 nm beyond $\sim 10^{13}$ W/cm^2 also indicates the saturation effects [64]. For intensities higher than 1×10^{14} W/cm^2, the energy transfer exhibits an abrupt increase, indicating the onset of material laser-induced dielectric breakdown, as outlined in Sec. III D.

Next, we analyze the residual energy of excited electrons at 800 and 400 nm beyond the pulse duration. The residual energy per excited electron (E^e_{res}) is obtained by dividing the energy (Fig. 1) by the number of excited electrons [64] at their saturation values. The results for 400 and 800 nm are shown in Fig. 3, highlighting the dominant excitation mechanisms at different intensity regimes. At 400 nm, E^e_{res} is approximately 3.10 eV for intensities up to $\approx 5 \times 10^{11}$ W/cm^2 (region A), indicating single photon absorption referred in Fig. 2. For higher intensities in region B, E^e_{res} increases potentially due to higher-order multiphoton absorption and secondary excitation of excited electrons [65,66]. In comparison, no excited electrons are observed at 800 nm until the intensity reaches 1×10^{10} W/cm^2 (region I). However, it approaches twice the photon energy (3.10 eV) for intensities ranging from 1×10^{10} W/cm^2 to 1×10^{12} W/cm^2 highlighted as region II, indicating ionization by two-photon absorption. E^e_{res} gradually increases above a 3.10 eV reference line for intensities larger than $\approx 1 \times 10^{12}$ W/cm^2 in Fig. 3, as a result of excitation via ionized free carriers and ionization due to electron tunneling across the barrier (region III). These observations are consistent with different interaction regimes illustrated in Fig. 2.

The Keldysh parameter, denoted by γ, serves as an approximate measure to determine the type of strong field ionization [65]. The Keldysh parameter for the interaction of a laser pulse of frequency ω and field amplitude E_0 with a material of energy gap Δ is given by

$$\gamma = \frac{\omega\sqrt{m\Delta}}{eE_0}, \tag{7}$$

where the electric field amplitude $E_0[\text{V/cm}] = 27.44\sqrt{I[\text{W/cm}^2]}$, I is the peak intensity of the laser pulse, and e and m are the charge and mass of electron, respectively. The condition $\gamma > 1$ represents multiphoton ionization being the primary mechanism of ionization, whereas $\gamma < 1$ indicates that tunneling ionization dominates. As the intensity of the laser pulse increases, a transition from multiphoton absorption to tunneling ionization can be observed. The Keldysh parameter at 800 nm is calculated at different peak intensities. Based on the value of γ, the intensities over which multiphoton or tunneling ionization dominate are highlighted in Fig. 2. When $I \approx 9 \times 10^{12}$ W/cm^2, the Keldysh parameter assumes a value of 1. It indicates that, for 800 nm, below an intensity of 9×10^{12} W/cm^2, the ionization is predominantly via multiphoton absorption and tunneling ionization above it.

B. Saturation of photoinduced current at 400 nm

Figures 4(a)–4(e) show the induced current for 30 fs, 400 nm laser pulses in the increasing order of incident peak

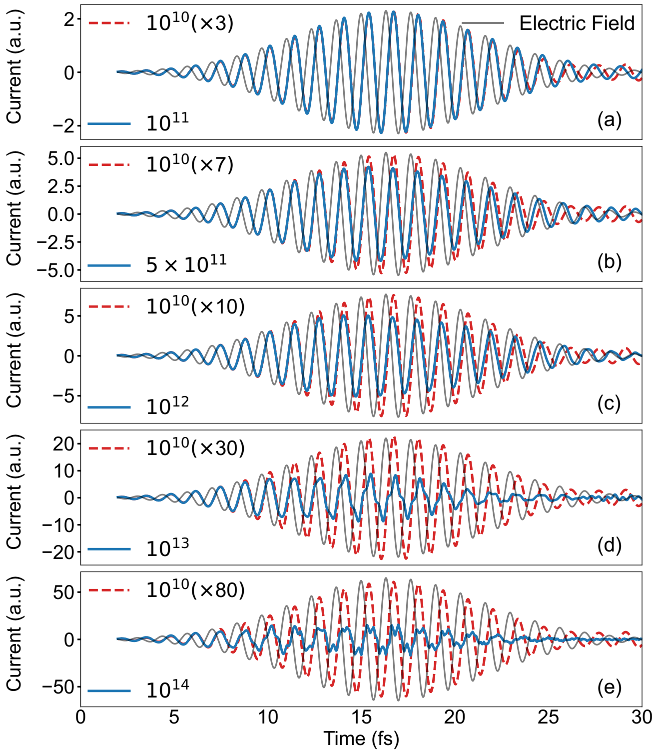

FIG. 4. Current profiles for 400 nm, 30 fs laser pulses showing the saturation effects. Panels (a)–(e) show the induced current in the order of increasing peak intensity from $I_0 = 1 \times 10^{11}$ W/cm^2 to $I_0 = 1 \times 10^{14}$ W/cm^2. The blue curves represent the induced current for $I_0 \geqslant 10^{11}$ W/cm^2, while the dashed red curve represents the current at $I_0 = 1 \times 10^{10}$ W/cm^2 taken as the weak reference current for comparison. The reference current is multiplied by a factor (given in braces) such that the difference between currents at weak and strong field strengths indicates nonlinear effects. The gray solid curve is the electric field of the laser pulse (normalized with respect to the magnitude of the current) given as a reference. It is observed that the photocurrent at 400 nm saturates at higher intensities, which is a typical nonlinear effect that occurs due to ground state bleaching due to linear absorption.

intensity from $I_0 = 1 \times 10^{11}$ W/cm^2 (a) to $I_0 = 1 \times 10^{14}$ W/cm^2 (e). The electric field of the laser pulse is also shown in the figure for reference. We take the current at $I_0 = 1 \times 10^{10}$ W/cm^2 as the reference (weak) current to discuss the dynamics at different intensities. For different peak intensities shown in Figs. 4(a)–4(e), the reference current is multiplied by a suitable factor so that the difference between currents at weak and strong field strengths indicates the nonlinear interaction. When the response is linear, the currents for weak and strong intensities will coincide and show similar profiles.

In Fig. 4(a), the time evolution of the current at $I_0 = 1 \times 10^{11}$ W/cm^2 follows the driving laser field and it coincides with the reference current, indicating a linear response. The response is dielectriclike: the current is $\pi/2$ phase shifted with the electric field $\boldsymbol{E}(t)$. For $I_0 > 1 \times 10^{11}$ W/cm^2 shown in Figs. 4(b)–4(e), the current for each peak intensity is initially very close to that of the reference current. However, as the electric field of the pulse increases, the current gradually becomes weaker than expected from the linear response. The deviation from the linear response, qualitatively indicated by the multiplication factor referred to above, successively increases as the peak intensity is increased through $I_0 = 5 \times 10^{11}$ W/cm^2 to $I_0 = 1 \times 10^{14}$ W/cm^2. This nonlinear effect of suppression of induced current occurs due to the bleaching of valence band electrons by absorption at 400 nm [5,7]. The majority of valence electrons are already excited and the conduction bands are mostly filled, resulting in the suppression of further electron excitation. Additionally, because the frequency of the applied laser pulse is higher than the band gap value, a significant current remains after the incident pulse has ended.

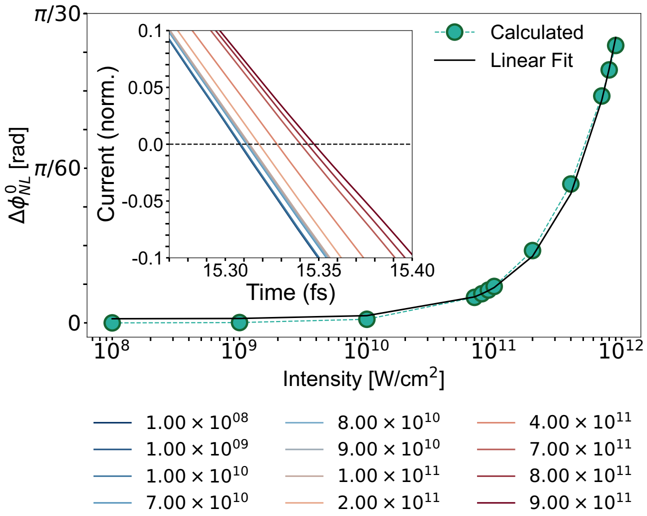

FIG. 5. Intensity scaling of the phase shift of current at 800 nm is shown. Phase shift is calculated by taking the current at 1×10^8 W/cm^2 as the reference. The phase shift is determined from the temporal shift of the induced current calculated at the zero crossing after the peak of the pulse ($\Delta\phi^0_{NL}$), as illustrated in the Supplemental Material figure [67]. In the inset, the induced current in the region close to the zero crossing is zoomed in, highlighting the temporal shift. The phase shift can be related to the optical Kerr effect, according to which the increase in phase shift is proportional to the peak intensity: $\Delta\phi^0_{NL} = m \times I_0$. From a linear fit of $\Delta\phi^0_{NL}$ versus I_0 (black solid line), the nonlinear refractive index $n_2 = 3.54 \times 10^{-11}$ cm^2/W is extracted.

C. Nonlinear refractive index change

The phase shift of light-induced current at 800 nm is depicted for various intensities in Fig. 5 with the current at 1×10^8 W/cm^2 taken as the reference. For a pulse of a given peak intensity, the induced current in the initial part of the pulse is in phase with the reference current. However, as the electric field of the pulse increases, the induced current starts accumulating a phase shift. The accumulated phase shift calculated from the temporal shift at the zero crossing after the peak of the pulse ($\Delta\phi^0_{NL}$) [67] in Fig. 5 increases as the peak intensity is increased. The phase shift can be related to the optical Kerr effect where the optical material density is proportional to the intensity envelope of the driving field [28,68]. Therefore, the increase in phase shift can be described as a linear rise with intensity, fitting exceptionally well to

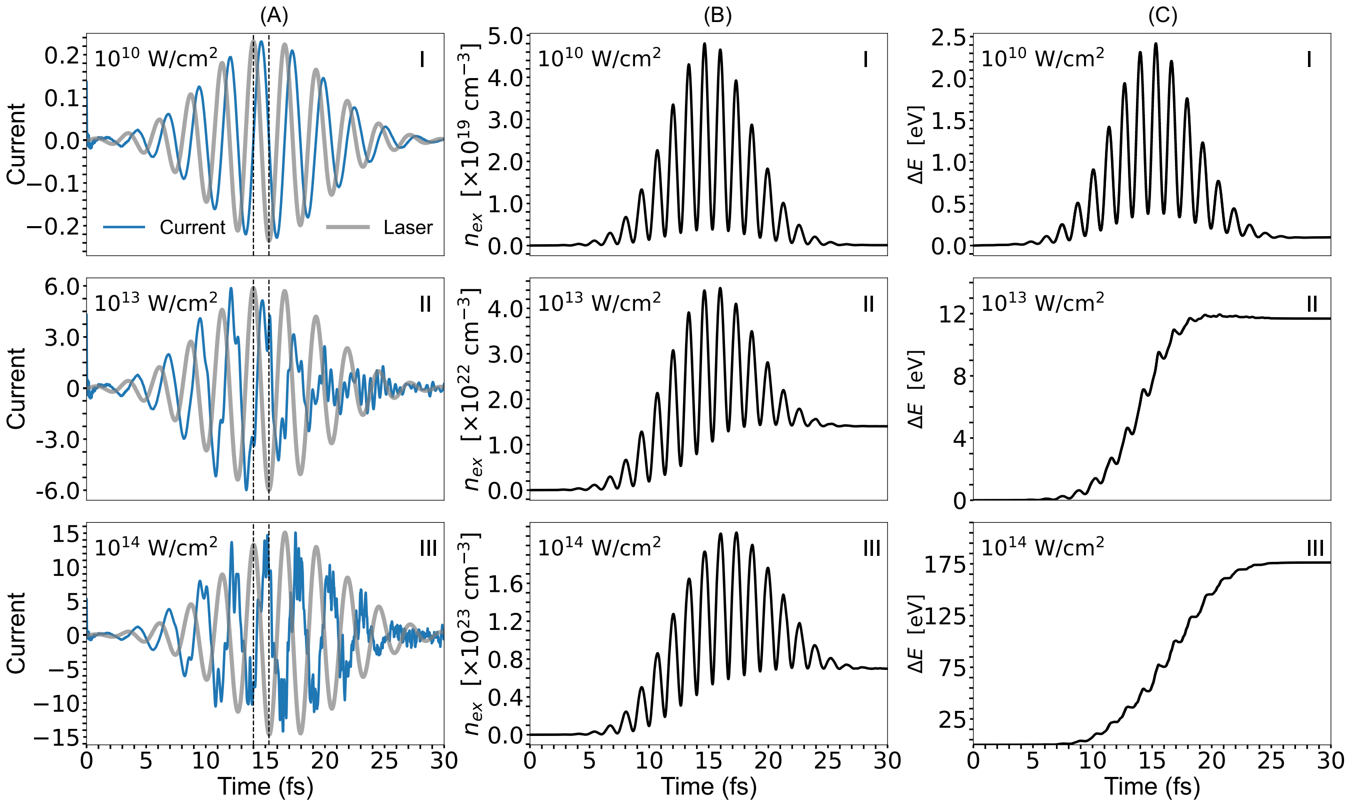

FIG. 6. Different regimes of the interaction of TiO$_2$ with 30 fs laser pulses at 800 nm with peak intensities 10^{10} W/cm^2 (top), 10^{13} W/cm^2 (middle), and 10^{14} W/cm^2 (bottom). Panel A(I–III) displays the induced current density and electric field (scaled with respect to the current amplitude to show phase relations). Panel B(I–III) shows the number density of excited electrons per cubic centimeter and panel C(I–III) represents the excitation energy. Dashed vertical lines in A(I–III) are given as a guide to the eye to show the phase variations.

the equation $\Delta\phi_{NL}^0 = m \times I_0$. The result of the fit is shown in Fig. 5 with a black solid line, from which we obtain the slope $m = 1.06 \times 10^{-13}$ cm^2/W. Using the relation $m = k l n_2$, where $k = 2\pi/\lambda$ and $l = 3.79$ Å, the propagation length, the nonlinear refractive index $n_2 = 3.54 \times 10^{-11}$ cm^2/W, can be extracted for 800 nm, 30 fs pulses.

D. Onset of dielectric breakdown

In Fig. 6, we present the time evolution of current, energy, and excited electron density for three different peak intensities, $I_0 = 10^{10}$, 10^{13}, and 10^{14} W/cm^2. The laser frequency is $\omega = 1.55$ eV (800 nm) and the pulse duration is $T = 30$ fs. The time profiles of the electric field and the induced current are depicted in Fig. 6 A(I–III). The electric field profile is normalized with respect to the peak of the induced current at a given peak intensity to enable a comparison of the relative phase. Figure 6 B(I–III) presents the number of excited electrons calculated using Eq. (5), while Fig. 6 C(I–III) depicts the excitation energy defined in Eq. (4) as a function of time.

The induced current at intensities 1×10^{10} W/cm^2 [Fig. 6 A(I)] follows the pulse's electric field with a phase shift of $\pi/2$, indicating a linear dielectric response. The excited electron density [Fig. 6 B(I)] and excitation energy [Fig. 6 C(I)] at this intensity oscillate synchronously with the electric field and the ground state conditions are restored after the interaction. The situation changes significantly at intensities of 10^{13} W/cm^2 and 10^{14} W/cm^2. The induced current during the interaction is distorted [Figs. 6 A(II) and A(III)] and the phase difference between the applied electric field and the induced current deviates from $\pi/2$. For $I = 1 \times 10^{14}$ W/cm^2, the current and the electric field become nearly out of phase, indicating a strongly nonlinear response of electrons to the incident field [4]. Starting from about 10 fs, the number of excited electrons and the excitation energy increase rapidly at 10^{13} W/cm^2 [Figs. 6 B(II) and C(II)] and 10^{14} W/cm^2 [Figs. 6 B(III) and C(III)]. By 20 fs, these quantities reach saturation values. Even after the laser pulse ends, the oscillation of the induced current persists, which is a clear indication of the onset of optical breakdown [53]. This behavior is consistent with the abrupt increase in energy discussed in Sec. III A due to resonant energy transfer at the breakdown. However, such oscillations will eventually decay due to dissipative processes such as electron-phonon coupling, impurity, and disorder scattering on longer time scales ($\gtrsim$100 fs) [12].

Electrons excited into the conduction band exhibit a metallic response, resulting in a collective plasmon mode. The plasma frequency corresponding to an electron density n_e can be estimated by

$$\omega_p = \left(\frac{n_e e^2}{m\epsilon}\right)^{1/2}, \tag{8}$$

where ϵ is the dielectric constant of anatase TiO$_2$ ($\epsilon = 5.82$) [69] and m and e are the mass and charge of the electron, respectively.

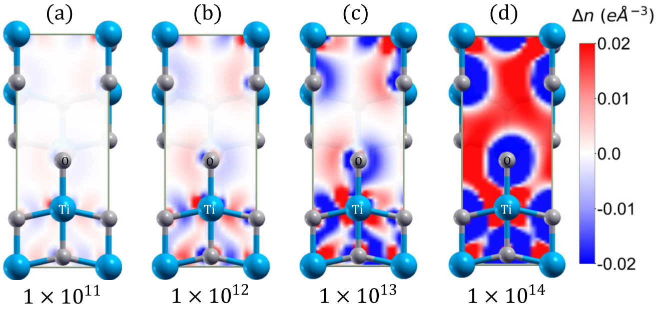

FIG. 7. Snapshots of electron density difference with respect to the unperturbed state evaluated for different intensities. The snapshots displayed here for various peak intensities are taken at the same instant of time when the electric field of the pulse reaches zero right after its peak value. The red and blue colors indicate the gain and the loss of the density, respectively, with respect to the ground state.

TABLE I. Summary of available experimental data for the nonlinear refractive index (n_2) of TiO_2 measured using ns and fs laser pulses at different wavelengths. The n_2 calculated in this work from TDDFT simulation is also given in the table for comparison.

n_2 (cm^2/W)	λ (nm)	Pulse width	Ref.
$\sim 10^{-14}$	532, 780	35 fs	[73]
6.32×10^{-13}	800	50 fs	[74]
2.0×10^{-14}	800	50 fs	[44]
1.0×10^{-15}	800	60 fs	[75]
2.5×10^{-11}	800	250 fs	[41]
6.2×10^{-11}	800	250 fs	[76]
1.2×10^{-13}	532	5 ns	[77]
1.5×10^{-13}	532	7 ns	[78]
3.54×10^{-11}	800	30 fs	This work

At an intensity 1×10^{13} W/cm^2, the final number of excited electrons [Fig. 6 B(II)] is 1.4×10^{22} cm^{-3}. This corresponds to a plasma frequency of $\omega_p = 1.82$ eV, which is slightly higher than the frequency of the applied laser pulse ($\omega_l = 1.55$ eV). As the intensity of the applied field increases, the density of electrons excited via the two-photon and tunneling mechanisms in the conduction band also gradually increases. When the electron density reaches a threshold where the plasma and laser frequencies are in resonance, a significant energy transfer occurs from the laser to the electrons. The low-amplitude coherent oscillations of the induced current observed on the trailing edge of the laser pulse [Figs. 6 A(II) and A(III)] result from the partial coherence between the involved nonstationary states left by the laser field. It is characteristic of plasmonic metal systems [70]. This ultrafast and dissipative strong-field transition to plasmonic metal-like behavior is known as dynamic metallization [23,71,72]. Based on the dynamics presented in Fig. 2 and in Fig. 6, $I_0 = 1 \times 10^{13}$ W/cm^2 can be identified as the intensity at which the laser-induced damage starts. For 30 fs pulses (11.7 fs FWHM), this intensity corresponds to a damage threshold of 0.1 J/cm^2.

The dynamics outlined in the preceding section are represented by the change in electron density induced by the laser pulse in Fig. 7. The snapshots displayed here for various peak intensities indicate the difference in electron density between the perturbed and unperturbed systems at the instant when the electric field of the pulse reaches zero right after its peak value. The positive (increase from the ground state) and the negative (reduction from the ground state) variations in the density are denoted in Figs. 7(c) and 7(d) by red and blue, respectively. When the laser is weak [Figs. 7(a) and 7(b)], the variation of electron density around ionic cores is uniform corresponding to a linear and adiabatic response. At higher laser intensity [Figs. 7(c) and 7(d)], the charge distribution extends into the interstitial region, indicating the laser-induced population of delocalized conduction band levels [34].

E. Comparison with experiments

We compare the figures estimated in the current work for TiO_2's nonlinear refractive index (n_2) and laser-induced damage threshold (LIDT) with those found in the literature. The experimental literature on the value of n_2 and LIDT of TiO_2 are summarized in Table I and Table II, respectively. The value of n_2 calculated in the present work for 30 fs pulses at 800 nm is about three orders greater than that measured using identical wavelength and pulse widths [73]. Similarly, the LIDT calculated from our simulation is smaller than the corresponding experimental data.

The difference between the experimental and computed values of n_2 and LIDT can be attributed to many factors. The duration and frequency of the laser pulse significantly impact the observed value of n_2 and LIDT, as implied by the variability of experimental data. It is important to note that most of the reported n_2 measurements of TiO_2 are performed on thin films, whereas simulations described here are for the bulk phase of TiO_2. The TDDFT formalism used for the present work considers only the dynamics of the electrons in the material, whereas the ions are kept fixed at their equilibrium positions in their ground state. Ionic dynamics induced by the laser pulse and its role in the collisional relaxation of the excitation are not considered in the current work. Next, using the PBE functional as an approximation to the XC energy can potentially contribute to the discrepancy. We obtain a direct band gap of 2.25 eV for TiO_2 using PBE, which is underestimated compared to accepted experimental values [81–85]. Using more accurate functionals leads to a larger band gap [57,86–88]. This translates to a higher threshold for two-photon absorption and, hence, the response will be dielectriclike for a larger range of peak intensities than observed in the present work. Consequently, the onset of material damage

TABLE II. Measured value of the laser-induced damage threshold (LIDT) of TiO_2 available in the literature. The table also lists the LIDT calculated in the present work using TDDFT simulations.

LIDT (J/cm^2)	λ (nm)	Pulse width	Ref.
0.5	800	50 fs	[79]
0.6	800	220 fs	[79]
1.43	532	10 ns	[80]
2.09	1064	10 ns	[80]
0.1	800	30 fs	This work

will shift to higher peak intensities, resulting in a higher damage threshold in agreement with the trend of the experimental data. In addition, experimental effects originating due to different sizes and volume fractions of synthesized materials, the effect of structure confinement in the case of nanostructured compounds, the dispersion of nonlinear refraction dispersion, etc., can also be significant, which are completely ignored in our calculations. Improving the agreement with experiments will require further calculations to understand the effect of band gap, to disentangle the contribution from ions and electrons [18,27], to incorporate thin-film geometries [6,89], and also include optical propagation effects [90].

IV. SUMMARY

We presented a systematic investigation of perturbative and nonperturbative electron dynamics of TiO_2 to 30 fs laser pulses at 400 nm and 800 nm using *ab initio* time-dependent density functional theory. The mechanism of nonlinear optical interaction of TiO_2 at different intensities is discussed. We can see the onset of laser-induced material damage and the accompanying plasmon dynamics from first principles. The trends of the value of the nonlinear refractive index (n_2) and laser-induced damage threshold obtained from the simulations are consistent with the experimental data in the literature. Nonresonant, perturbative interactions at 800 nm and the accompanying nonlinear phase shift observed in TiO_2 well below the damage threshold hold promises incorporating TiO_2 in optical switches. The present study could guide the further exploration of laser parameters and structural and defect engineering of TiO_2 with tailored properties for specific applications, potentially leading to improved performance in nonlinear photonics devices. By pursuing these directions, researchers can advance the understanding and utilization of TiO_2 and similar materials for nonlinear photonics applications.

ACKNOWLEDGMENTS

This work was in part supported by the Center for Advanced Systems Understanding (CASUS), which is financed by Germany's Federal Ministry of Education and Research (BMBF) and by the Saxon state government out of the state budget approved by the Saxon State Parliament. We also acknowledge the Helmholtz Information and Data Science Academy (HIDA) for providing financial support, enabling a short-term research stay at the Center for Advanced Systems Understanding, Helmholtz-Zentrum Dresden-Rossendorf (HZDR) to carry out the simulations.

[1] E. Runge and E. K. U. Gross, Density-functional theory for time-dependent systems, Phys. Rev. Lett. **52**, 997 (1984).
[2] G. F. Bertsch, J.-I. Iwata, A. Rubio, and K. Yabana, Real-space, real-time method for the dielectric function, Phys. Rev. B **62**, 7998 (2000).
[3] K. Yabana, T. Sugiyama, Y. Shinohara, T. Otobe, and G. F. Bertsch, Time-dependent density functional theory for strong electromagnetic fields in crystalline solids, Phys. Rev. B **85**, 045134 (2012).
[4] A. Yamada and K. Yabana, Energy transfer from intense laser pulse to dielectrics in time-dependent density functional theory, Eur. Phys. J. D **73**, 87 (2019).
[5] M. Uemoto, Y. Kuwabara, S. A. Sato, and K. Yabana, Nonlinear polarization evolution using time-dependent density functional theory, J. Chem. Phys. **150**, 094101 (2019).
[6] M. Uemoto, S. Kurata, N. Kawaguchi, and K. Yabana, First-principles study of ultrafast and nonlinear optical properties of graphite thin films, Phys. Rev. B **103**, 085433 (2021).
[7] A. Hashmi, S. Yamada, A. Yamada, K. Yabana, and T. Otobe, Nonlinear dynamics of electromagnetic field and valley polarization in WSe_2 monolayer, Appl. Phys. Lett. **120**, 051108 (2022).
[8] N. Tancogne-Dejean, O. D. Mücke, F. X. Kärtner, and A. Rubio, Impact of the electronic band structure in high-harmonic generation spectra of solids, Phys. Rev. Lett. **118**, 087403 (2017).
[9] I. Floss, C. Lemell, G. Wachter, V. Smejkal, S. A. Sato, X.-M. Tong, K. Yabana, and J. Burgdörfer, Ab initio multiscale simulation of high-order harmonic generation in solids, Phys. Rev. A **97**, 011401(R) (2018).
[10] T. Otobe, First-principle description for the high-harmonic generation in a diamond by intense short laser pulse, J. Appl. Phys. **111**, 093112 (2012).
[11] M. S. Mrudul, N. Tancogne-Dejean, A. Rubio, and G. Dixit, High-harmonic generation from spin-polarised defects in solids, npj Comput. Mater. **6**, 10 (2020).
[12] G. Wachter, C. Lemell, J. Burgdörfer, S. A. Sato, X.-M. Tong, and K. Yabana, Ab initio simulation of electrical currents induced by ultrafast laser excitation of dielectric materials, Phys. Rev. Lett. **113**, 087401 (2014).
[13] G. Wachter, S. A. Sato, I. Floss, C. Lemell, X.-M. Tong, K. Yabana, and J. Burgdörfer, Controlling ultrafast currents by the nonlinear photogalvanic effect, New J. Phys. **17**, 123026 (2015).
[14] U. De Giovannini, H. Hübener, and A. Rubio, Monitoring electron-photon dressing in WSe_2, Nano Lett. **16**, 7993 (2016).
[15] H. Hübener, M. A. Sentef, U. De Giovannini, A. F. Kemper, and A. Rubio, Creating stable Floquet–Weyl semimetals by laser-driving of 3D Dirac materials, Nat. Commun. **8**, 13940 (2017).
[16] S. A. Sato, K. Yabana, Y. Shinohara, T. Otobe, K.-M. Lee, and G. F. Bertsch, Time-dependent density functional theory of high-intensity short-pulse laser irradiation on insulators, Phys. Rev. B **92**, 205413 (2015).
[17] S. A. Sato and K. Yabana, First-principles calculations for initial electronic excitation in dielectrics induced by intense femtosecond laser pulses, in *Proceedings Volume 10014, Laser-Induced Damage in Optical Materials 2016* (SPIE, Bellingham, WA, 2016), Vol. 10014, pp. 155–161.
[18] A. Niedermayr, M. Volkov, S. A. Sato, N. Hartmann, Z. Schumacher, S. Neb, A. Rubio, L. Gallmann, and U. Keller, Few-femtosecond dynamics of free-free opacity in optically heated metals, Phys. Rev. X **12**, 021045 (2022).
[19] Y. Shimotsuma, K. Kinouchi, R. Yanoshita, M. Fujiwara, N. Mizuochi, N. Mizuochi, M. Uemoto, M. Shimizu, and K.

Miura, Formation of NV centers in diamond by a femtosecond laser single pulse, Opt. Express **31**, 1594 (2023).

[20] S. Ghimire, A. D. DiChiara, E. Sistrunk, P. Agostini, L. F. DiMauro, and D. A. Reis, Observation of high-order harmonic generation in a bulk crystal, Nat. Phys. **7**, 138 (2011).

[21] M. Schultze, E. M. Bothschafter, A. Sommer, S. Holzner, W. Schweinberger, M. Fiess, M. Hofstetter, R. Kienberger, V. Apalkov, V. S. Yakovlev *et al.*, Controlling dielectrics with the electric field of light, Nature (London) **493**, 75 (2013).

[22] O. Schubert, M. Hohenleutner, F. Langer, B. Urbanek, C. Lange, U. Huttner, D. Golde, T. Meier, M. Kira, S. W. Koch *et al.*, Sub-cycle control of terahertz high-harmonic generation by dynamical bloch oscillations, Nat. Photon. **8**, 119 (2014).

[23] M. Durach, A. Rusina, M. F. Kling, and M. I. Stockman, Predicted ultrafast dynamic metallization of dielectric nanofilms by strong single-cycle optical fields, Phys. Rev. Lett. **107**, 086602 (2011).

[24] A. Schiffrin, T. Paasch-Colberg, N. Karpowicz, V. Apalkov, D. Gerster, S. Mühlbrandt, M. Korbman, J. Reichert, M. Schultze, S. Holzner *et al.*, Optical-field-induced current in dielectrics, Nature (London) **493**, 70 (2013).

[25] M. Lucchini, S. A. Sato, A. Ludwig, J. Herrmann, M. Volkov, L. Kasmi, Y. Shinohara, K. Yabana, L. Gallmann, and U. Keller, Attosecond dynamical Franz-Keldysh effect in polycrystalline diamond, Science **353**, 916 (2016).

[26] V. Apalkov and M. I. Stockman, Metal nanofilm in strong ultrafast optical fields, Phys. Rev. B **88**, 245438 (2013).

[27] M. Schultze, K. Ramasesha, C. Pemmaraju, S. A. Sato, D. Whitmore, A. Gandman, J. S. Prell, L. J. Borja, D. Prendergast, K. Yabana *et al.*, Attosecond band-gap dynamics in silicon, Science **346**, 1348 (2014).

[28] A. Sommer, E. M. Bothschafter, S. A. Sato, C. Jakubeit, T. Latka, O. Razskazovskaya, H. Fattahi, M. Jobst, W. Schweinberger, V. Shirvanyan *et al.*, Attosecond nonlinear polarization and light–matter energy transfer in solids, Nature (London) **534**, 86 (2016).

[29] S. Sederberg, D. Zimin, S. Keiber, F. Siegrist, M. S. Wismer, V. S. Yakovlev, I. Floss, C. Lemell, J. Burgdörfer, M. Schultze *et al.*, Attosecond optoelectronic field measurement in solids, Nat. Commun. **11**, 430 (2020).

[30] M. Durach, A. Rusina, M. F. Kling, and M. I. Stockman, Metallization of nanofilms in strong adiabatic electric fields, Phys. Rev. Lett. **105**, 086803 (2010).

[31] V. Apalkov and M. I. Stockman, Theory of dielectric nanofilms in strong ultrafast optical fields, Phys. Rev. B **86**, 165118 (2012).

[32] O. Kwon, T. Paasch-Colberg, V. Apalkov, B.-K. Kim, J.-J. Kim, M. I. Stockman, and D. Kim, Semimetallization of dielectrics in strong optical fields, Sci. Rep. **6**, 21272 (2016).

[33] G. Su, L. Jiang, F. Wang, L. Qu, and Y. Lu, First-principles simulations for excitation of currents in linear carbon chains under femtosecond laser pulse irradiation, Phys. Lett. A **380**, 2453 (2016).

[34] X. Zhang, F. Wang, L. Jiang, and Y. Yao, Manipulation of the dielectric properties of diamond by an ultrashort laser pulse, Phys. Rev. B **95**, 184301 (2017).

[35] A. Kazempour, T. Morshedloo, and F. Wang, Transient nonlinear optics of diamond under ultrashort excitation pulses, Appl. Phys. A **127**, 44 (2021).

[36] C. Wang, L. Jiang, X. Li, F. Wang, Y. Yuan, L. Qu, and Y. Lu, Nonlinear ionization mechanism dependence of energy absorption in diamond under femtosecond laser irradiation, J. Appl. Phys. **113**, 143106 (2013).

[37] R. Shinde and A. K. Singh, Nonlinear polarization and low-dissipation ultrafast optical switching in phosphorene, J. Phys. Chem. C **122**, 19146 (2018).

[38] X. Su, L. Jiang, F. Wang, G. Su, L. Qu, and Y. Lu, Electron dynamics and optical properties modulation of monolayer MoS_2 by femtosecond laser pulse: A simulation using time-dependent density functional theory, Appl. Phys. A **123**, 476 (2017).

[39] M. F. M. Rusdi, A. A. Latiff, M. C. Paul, S. Das, A. Dhar, H. Ahmad, and S. W. Harun, Titanium dioxide (TiO_2) film as a new saturable absorber for generating mode-locked Thulium-Holmium doped all-fiber laser, Opt. Laser Technol. **89**, 16 (2017).

[40] H. Ahmad, S. A. Reduan, Z. A. Ali, M. A. Ismail, N. E. Ruslan, C. S. J. Lee, R. Puteh, and S. W. Harun, C-band Q-switched fiber laser using titanium dioxide (TiO_2) as saturable absorber, IEEE Photon. J. **8**, 1 (2015).

[41] H. I. Elim, W. Ji, A. H. Yuwono, J. M. Xue, and J. Wang, Ultrafast optical nonlinearity in poly (methylmethacrylate)-TiO_2 nanocomposites, Appl. Phys. Lett. **82**, 2691 (2003).

[42] C. C. Evans, J. D. B. Bradley, E. A. Martí-Panameño, and E. Mazur, Mixed two- and three-photon absorption in bulk rutile (TiO_2) around 800 nm, Opt. Express **20**, 3118 (2012).

[43] T. Hashimoto, T. Yoko, and S. Sakka, Sol–gel preparation and third-order nonlinear optical properties of TiO_2 thin films, Bull. Chem. Soc. Jpn. **67**, 653 (1994).

[44] H. A. Castillo-Matadamas, R. M. Lima-García, and R. Quintero-Torres, Ultrafast nonlinear optical properties of TiO_2 nanoclusters at 850 nm, J. Mod. Opt. **57**, 1100 (2010).

[45] D. Milam, Review and assessment of measured values of the nonlinear refractive-index coefficient of fused silica, Appl. Opt. **37**, 546 (1998).

[46] O. Reshef, K. Shtyrkova, M. G. Moebius, S. Griesse-Nascimento, S. Spector, C. C. Evans, E. Ippen, and E. Mazur, Polycrystalline anatase titanium dioxide microring resonators with negative thermo-optic coefficient, J. Opt. Soc. Am. B **32**, 2288 (2015).

[47] J. D. B. Bradley, C. C. Evans, J. T. Choy, O. Reshef, P. B. Deotare, F. Parsy, K. C. Phillips, M. Lončar, and E. Mazur, Submicrometer-wide amorphous and polycrystalline anatase TiO_2 waveguides for microphotonic devices, Opt. Express **20**, 23821 (2012).

[48] J. T. Choy, J. D. B. Bradley, P. B. Deotare, I. B. Burgess, C. C. Evans, E. Mazur, and M. Lončar, Integrated TiO_2 resonators for visible photonics, Opt. Lett. **37**, 539 (2012).

[49] C. C. Evans, K. Shtyrkova, J. D. B. Bradley, O. Reshef, E. Ippen, and E. Mazur, Spectral broadening in anatase titanium dioxide waveguides at telecommunication and near-visible wavelengths, Opt. Express **21**, 18582 (2013).

[50] N. Tancogne-Dejean, M. J. Oliveira, X. Andrade, H. Appel, C. H. Borca, G. Le Breton, F. Buchholz, A. Castro, S. Corni, A. A. Correa *et al.*, Octopus, a computational framework for exploring light-driven phenomena and quantum dynamics in extended and finite systems, J. Chem. Phys. **152**, 124119 (2020).

[51] G. Vignale and W. Kohn, Current-dependent exchange-correlation potential for dynamical linear response theory, Phys. Rev. Lett. **77**, 2037 (1996).

[52] D. Rappoport, N. R. M. Crawford, F. Furche, and K. Burke, Approximate density functionals: Which should I choose? in *Encyclopedia of Inorganic Chemistry* (John Wiley & Sons, Ltd, Chichester, England, UK, 2005).

[53] T. Otobe, M. Yamagiwa, J.-I. Iwata, K. Yabana, T. Nakatsukasa, and G. F. Bertsch, First-principles electron dynamics simulation for optical breakdown of dielectrics under an intense laser field, Phys. Rev. B **77**, 165104 (2008).

[54] J. K. Burdett, T. Hughbanks, G. J. Miller, J. W. Richardson, Jr., and J. V. Smith, Structural-electronic relationships in inorganic solids: Powder neutron diffraction studies of the rutile and anatase polymorphs of titanium dioxide at 15 and 295 K, J. Am. Chem. Soc. **109**, 3639 (1987).

[55] K. V. K. Rao, S. V. N. Naidu, and L. Iyengar, Thermal expansion of rutile and anatase, J. Am. Ceram. Soc. **53**, 124 (1970).

[56] C. J. Howard, T. M. Sabine, and F. Dickson, Structural and thermal parameters for rutile and anatase, Acta Crystallogr. B: Struct. Sci. **47**, 462 (1991).

[57] S. L. S. B., M. D., M. Posselt, A. A. S. Devi, and A. Sharan, Modified HSE06 functional applied to anatase TiO_2: Influence of exchange fraction on the quasiparticle electronic structure and optical response, Electron. Struct. **4**, 045001 (2022).

[58] L. Kleinman and D. M. Bylander, Efficacious form for model pseudopotentials, Phys. Rev. Lett. **48**, 1425 (1982).

[59] J. P. Perdew, K. Burke, and M. Ernzerhof, Generalized gradient approximation made simple, Phys. Rev. Lett. **77**, 3865 (1996).

[60] H. J. Monkhorst and J. D. Pack, Special points for Brillouin-zone integrations, Phys. Rev. B **13**, 5188 (1976).

[61] A. Castro, M. A. L. Marques, and A. Rubio, Propagators for the time-dependent Kohn–Sham equations, J. Chem. Phys. **121**, 3425 (2004).

[62] M. Thiele, E. K. U. Gross, and S. Kümmel, Adiabatic approximation in nonperturbative time-dependent density-functional theory, Phys. Rev. Lett. **100**, 153004 (2008).

[63] See Supplemental Material at http://link.aps.org/supplemental/10.1103/PhysRevB.108.195149 for the GGA (PBE) electronic band structure of anatase TiO_2.

[64] See Supplemental Material at http://link.aps.org/supplemental/10.1103/PhysRevB.108.195149 for the number of excited electrons in TiO_2 at their saturation values created when interacting with 800 nm and 400 nm laser pulses at different peak intensities.

[65] L. Keldysh *et al.*, Ionization in the field of a strong electromagnetic wave, Zh. Eksp. Teor. Fiz. **47**, 1945 (1965) [Sov. Phys. JETP **20**, 1307 (1965)].

[66] H. R. Reiss, Effect of an intense electromagnetic field on a weakly bound system, Phys. Rev. A **22**, 1786 (1980).

[67] See Supplemental Material at http://link.aps.org/supplemental/10.1103/PhysRevB.108.195149 for the phase shift of photoinduced current accumulated during the interaction of TiO_2 with 800 nm pulses of different peak intensities.

[68] A. M. Sommer, *Ultrafast Strong Field Dynamics in Dielectrics* (Springer, New York, 2016).

[69] R. J. Gonzalez, R. Zallen, and H. Berger, Infrared reflectivity and lattice fundamentals in anatase TiO_2s, Phys. Rev. B **55**, 7014 (1997).

[70] X. Zhang, F. Wang, Z. Liu, X. Feng, and S. Pang, Controlling energy transfer from intense ultrashort light pulse to crystals: A comparison study in attosecond and femtosecond regimes, Phys. Lett. A **384**, 126710 (2020).

[71] M. I. Stockman, S. V. Faleev, and D. J. Bergman, Coherent control of femtosecond energy localization in nanosystems, Phys. Rev. Lett. **88**, 067402 (2002).

[72] M. I. Stockman and P. Hewageegana, Absolute phase effect in ultrafast optical responses of metal nanostructures, Appl. Phys. A **89**, 247 (2007).

[73] L.-H. Guo, Y.-W. Wang, Y.-Q. Jiang, S. Xiao, and J. He, Dependence of nonlinear optical response of anatase TiO_2 on shape and excitation intensity, Chin. Phys. Lett. **34**, 077803 (2017).

[74] H. Long, A. Chen, G. Yang, Y. Li, and P. Lu, Third-order optical nonlinearities in anatase and rutile TiO_2 thin films, Thin Solid Films **517**, 5601 (2009).

[75] E. Portuondo-Campa, A. Tortschanoff, F. van Mourik, and M. Chergui, Ultrafast nonresonant response of TiO_2 nanostructured films, J. Chem. Phys. **128**, 244718 (2008).

[76] A. H. Yuwono, B. Liu, J. Xue, J. Wang, H. I. Elim, W. Ji, Y. Li, and T. J. White, Controlling the crystallinity and nonlinear optical properties of transparent TiO_2–PMMA nanohybrids, J. Mater. Chem. **14**, 2978 (2004).

[77] Y. Watanabe, M. Ohnishi, and T. Tsuchiya, Measurement of nonlinear absorption and refraction in titanium dioxide single crystal by using a phase distortion method, Appl. Phys. Lett. **66**, 3431 (1995).

[78] L. Irimpan, B. Krishnan, V. P. N. Nampoori, and P. Radhakrishnan, Luminescence tuning and enhanced nonlinear optical properties of nanocomposites of ZnO–TiO_2, J. Colloid Interface Sci. **324**, 99 (2008).

[79] J. Yao, Z. Fan, Y. Jin, Y. Zhao, H. He, and J. Shao, Investigation of damage threshold to TiO_2 coatings at different laser wavelength and pulse duration, Thin Solid Films **516**, 1237 (2008).

[80] S. Kumar, A. Shankar, N. Kishore, C. Mukherjee, R. Kamparath, and S. Thakur, Laser-induced damage threshold study on TiO_2/SiO_2 multilayer reflective coatings, Indian J. Phys. **94**, 105 (2020).

[81] H. Tang, H. Berger, P. E. Schmid, F. Lévy, and G. Burri, Photoluminescence in TiO_2 anatase single crystals, Solid State Commun. **87**, 847 (1993).

[82] H. Tang, F. Lévy, H. Berger, and P. E. Schmid, Urbach tail of anatase TiO_2, Phys. Rev. B **52**, 7771 (1995).

[83] L. Kavan, M. Grätzel, S. E. Gilbert, C. Klemenz, and H. J. Scheel, Electrochemical and photoelectrochemical investigation of single-crystal anatase, J. Am. Chem. Soc. **118**, 6716 (1996).

[84] N. Hosaka, T. Sekiya, M. Fujisawa, C. Satoko, and S. Kurita, UV reflection spectra of anatase TiO_2, J. Electron Spectrosc. Relat. Phenom. **78**, 75 (1996).

[85] N. Hosaka, T. Sekiya, C. Satoko, and S. Kurita, Optical properties of single-crystal anatase TiO_2, J. Phys. Soc. Jpn. **66**, 877 (1997).

[86] L. Chiodo, J. M. García-Lastra, A. Iacomino, S. Ossicini, J. Zhao, H. Petek, and A. Rubio, Self-energy and excitonic effects in the electronic and optical properties of TiO_2 crystalline phases, Phys. Rev. B **82**, 045207 (2010).

[87] M. Landmann, E. Rauls, and W. G. Schmidt, The electronic structure and optical response of rutile, anatase and brookite TiO_2, J. Phys.: Condens. Matter **24**, 195503 (2012).

[88] E. Baldini, L. Chiodo, A. Dominguez, M. Palummo, S. Moser, M. Yazdi-Rizi, G. Auböck, B. P. P. Mallett, H. Berger, A. Magrez, C. Bernhard, M. Grioni, A. Rubio, and M. Chergui,

Strongly bound excitons in anatase TiO_2 single crystals and nanoparticles, Nat. Commun. **8**, 13 (2017).

[89] K.-M. Lee, C. Min Kim, S. A. Sato, T. Otobe, Y. Shinohara, K. Yabana, and T. Moon Jeong, First-principles simulation of the optical response of bulk and thin-film α-quartz irradiated with an ultrashort intense laser pulse, J. Appl. Phys. **115**, 053519 (2014).

[90] S. Yamada, T. Otobe, D. Freeman, A. Kheifets, and K. Yabana, Propagation effects in high-harmonic generation from dielectric thin films, Phys. Rev. B **107**, 035132 (2023).